






Imaging the Milky Way with Millihertz Gravitational Waves

Kaitlyn Szekeczes¹, Scott Noble¹ , Cecilia Chirenti^{2,3,4,5} , and James Ira Thorpe¹ ¹ Gravitational Astrophysics Laboratory, NASA/GSFC, 8800 Greenbelt Road, Greenbelt, MD 20771, USA; james.i.thorpe@nasa.gov² Department of Astronomy, University of Maryland, College Park, MD 20742-2421, USA³ Astroparticle Physics Laboratory, NASA/GSFC, 8800 Greenbelt Road, Greenbelt, MD 20771, USA⁴ Center for Research and Exploration in Space Science and Technology, NASA/GSFC, Greenbelt, MD 20771, USA⁵ Center for Mathematics, Computation, and Cognition, UFABC, Santo André, SP 09210-170, Brazil

Received 2023 January 31; revised 2023 May 6; accepted 2023 May 8; published 2023 June 15

Abstract

Modern astronomers enjoy access to all-sky images across a wide range of the electromagnetic spectrum from long-wavelength radio to high-energy gamma rays. The most prominent feature in many of these images is our own Galaxy, with different features revealed in each wave band. Gravitational waves (GWs) have recently been added to the astronomers' toolkit as a nonelectromagnetic messenger. To date, all identified GW sources have been extra-Galactic and transient. However, the Milky Way hosts a population of ultracompact binaries (UCBs), which radiate persistent GWs in the milliHertz band that is not observable with today's terrestrial gravitational-wave detectors. Space-based detectors such as the Laser Interferometer Space Antenna will measure this population and provide a census of their location, masses, and orbital properties. In this work, we will show how this data can be used to form a false-color image of the Galaxy that represents the intensity and frequency of the gravitational waves produced by the UCB population. Such images can be used to study the morphology of the Galaxy, identify interesting multimessenger sources through cross-matching, and for educational and outreach purposes.

Unified Astronomy Thesaurus concepts: [Gravitational waves \(678\)](#); [Gravitational wave astronomy \(675\)](#); [White dwarf stars \(1799\)](#); [Compact binary stars \(283\)](#); [Astronomy image processing \(2306\)](#)

1. Introduction

Gravitational waves (GWs) are perturbations in spacetime described by Einstein (1918) which travel at the speed of light and carry energy, momentum, and information from their progenitor systems. In 2015, after decades of effort, the first direct detection of an astrophysical GW source was reported by Abbott et al. (2016). This discovery was made using the Laser Interferometric Gravitational-wave Observatory (LIGO; LIGO Scientific Collaboration 2015), an Earth-based instrument sensitive to GWs in the high-frequency band $10 \text{ Hz} \lesssim f \lesssim 1 \text{ kHz}$. Since then, LIGO and the European Virgo detector (Acernese et al. 2015) have combined to detect nearly 100 GW events (Abbott et al. 2023). All of these GW signals have been transient (<1 minute), representing the final inspiral and merger of the compact objects that produced them. They are also exclusively extra-Galactic, due to the fact that the observed phase of the binary systems' evolution represents a very small fraction of their overall lifespan, and hence such events occur infrequently in any given Galaxy. At lower frequencies, $f \sim 1 \text{ mHz}$, there exists a large population of persistent GW sources arising from binary compact objects in the Milky Way. These systems, collectively referred to as ultracompact binaries (UCBs), represent the end state of many binary stellar systems and include mixed pairs of black holes, neutron stars, white dwarfs, and evolved main-sequence stars (Belczynski et al. 2002; Yu & Jeffery 2010; Nissanke et al. 2012). Observing GWs in this frequency band requires space-based detectors, such as the European-US Laser Interferometer Space Antenna (Amaro-Seoane et al. 2017), or the Chinese TianQin

(Luo et al. 2016) and Taiji (Ruan et al. 2020) mission concepts, all of which aim to be operational in the 2030s. Population synthesis models estimate that LISA will observe tens of thousands of individual UCB systems in the Milky Way (Korol et al. 2022) and perhaps nearby satellite galaxies (Keim et al. 2023). A simultaneous global-fit pipeline, such as the one prototyped by Littenberg & Cornish (2023), will search LISA's data stream and produce a catalog of several tens of thousands of UCB sources with measured GW amplitudes, GW frequencies, and sky locations as well as derived physical properties such as luminosity distance, component masses, etc. This information can be used to conduct a wide array of scientific investigations on individual UCB systems, populations of UCB systems, and the Milky Way Galaxy itself as described in Chapter 1 of Amaro-Seoane et al. (2023) and references therein.

In this work, we show how it is also possible to study the Milky Way as an astrophysical object directly through the combined GW energy produced by its population of resolved UCBs. This is the GW analog to studying the Galaxy through the light produced by its population of stars. In Section 2 we summarize the Milky Way UCB population and review the process by which space-based detectors observe GWs from these systems and extract relevant astrophysical information. In particular, we describe how a simulated Galaxy would be observed by LISA and a notional second-generation space-based detector known as the Advanced MilliHertz Gravitational-wave Observatory (AMIGO), proposed by Baibhav et al. (2021), which improves on LISA's sensitivity by an order of magnitude across the measurement band. In Section 3 we describe our method of combining the individual GW observations to produce a false-color GW image. Finally in Section 4 we present our simulated images of the Milky Way with LISA and AMIGO.



Original content from this work may be used under the terms of the [Creative Commons Attribution 4.0 licence](#). Any further distribution of this work must maintain attribution to the author(s) and the title of the work, journal citation and DOI.

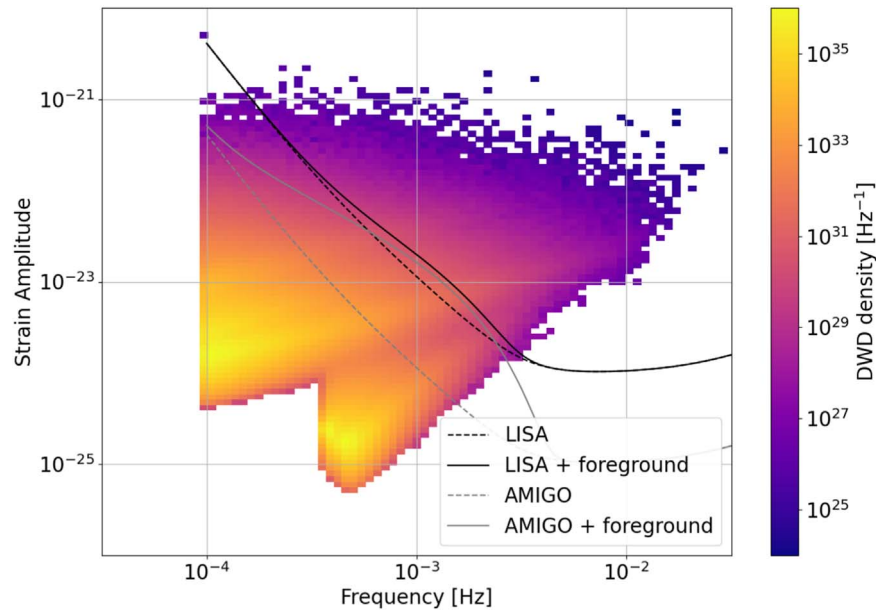


Figure 1. Number density of gravitationally-radiating UCBs in the LISA band in a simulated Milky Way population. The instrumental (dashed) and combined instrumental and confusion limits (solid) for a year of observation with the LISA and AMIGO missions are shown for comparison.

2. GW Observation of UCBs

2.1. The Galactic UCB Population in the mHz Band

Modeling the population of UCBs potentially observable by a milliHertz GW detector requires detailed treatment of Galactic structure, stellar initial mass functions, stellar and binary evolution, etc. Fortunately, a large body of research on this topic exists in part because of the need to assess the science case of the LISA mission, see Nelemans et al. (2001) and Wagg et al. (2022).

For this work, we use the simulated UCB population developed for the LISA Data Challenge round 1–4,⁶ which was first described by Toonen et al. (2012) and is further detailed in Korol et al. (2022). The simulated catalog consists of $\sim 3 \times 10^7$ UCB sources with individual GW frequencies, frequency derivatives, GW amplitudes, sky locations, and observable orbital elements (inclination, polarization, and orbital phase). Each of these parameters can potentially be measured through their effect on the GWs generated by individual systems. For this work, we focus on GW frequency (which corresponds to twice the orbital frequency of the UCB), GW amplitude (which is determined by the component masses, orbital separation, and luminosity distance), and the sky location. The density of UCB sources in the GW frequency/amplitude plane, ρ_{UCB} , for the LDC1–4 simulated Galaxy is plotted in Figure 1. The density is normalized by the frequency and amplitude bins such that the number of UCBs in an region of the frequency/amplitude plane is computed as

$$N_{\text{UCB}} = \int_{f_{\text{GW}}} \int_{A_{\text{GW}}} \rho_{\text{UCB}}(f, A) df_{\text{GW}} dA_{\text{GW}}. \quad (1)$$

Two distinct populations of UCB are visible, the detached UCB binaries make up the bulk of the overall population and have somewhat lower GW frequencies and higher GW amplitudes. The interacting UCB binaries represent systems potentially undergoing mass transfer (e.g., AM CVn, etc.) with

typically higher GW frequencies and lower GW amplitudes. The combined population is not modeled for GW frequencies below 9×10^{-5} Hz as such systems would likely not be detectable by LISA-like observatories.

2.2. Observing GWs with Space-based Interferometers

The sensitivity of GW instruments is typically expressed as equivalent GW strain, which for each frequency bin is the amount of GW amplitude that corresponds to the technical noise added by the instrument. This is the GW equivalent of dark noise in a CCD. For interferometric GW instruments, the equivalent strain is primarily determined by three factors. The physical size of the detector both sets the scale for the response to GW strain as well as the GW wavelength which optimally couples to the antenna and therefore the frequency of peak sensitivity. The sensitivity at frequencies below the peak sensitivity is primarily determined by the ability to reject nongravitational forces on fiducial test masses used to reference geodesic motion. Sensitivity at high frequencies is limited by the ability to sense length changes between these test masses, with a fundamental limit being shot noise, i.e., statistical fluctuations in the number of photons transmitted between the test masses. As the detector design matures, numerous other noise sources must be evaluated and their contributions to equivalent GW strain included. For the case of LISA, which is in the late stages of its final design at ESA, the estimated GW strain is quite mature and robust. For AMIGO, which does not have a reference design but is instead intended as an example of a next-generation space-based GW instrument, the equivalent GW strain estimate is entirely notional. The characteristic strain curves for LISA and AMIGO over a one year observation time are plotted as the dashed curves in Figure 1. Of the tens of millions of UCB systems producing GWs in the LISA band, tens of thousands will have amplitudes exceeding the instrumental sensitivity, making them potentially detectable. Since LISA is an effectively all-sky instrument, this leads to a “confusion problem” in which the observed GW radiation cannot be associated with a particular source. A subset of the

⁶ Data available at <https://lisa-ldc.lal.in2p3.fr/challenge1>.

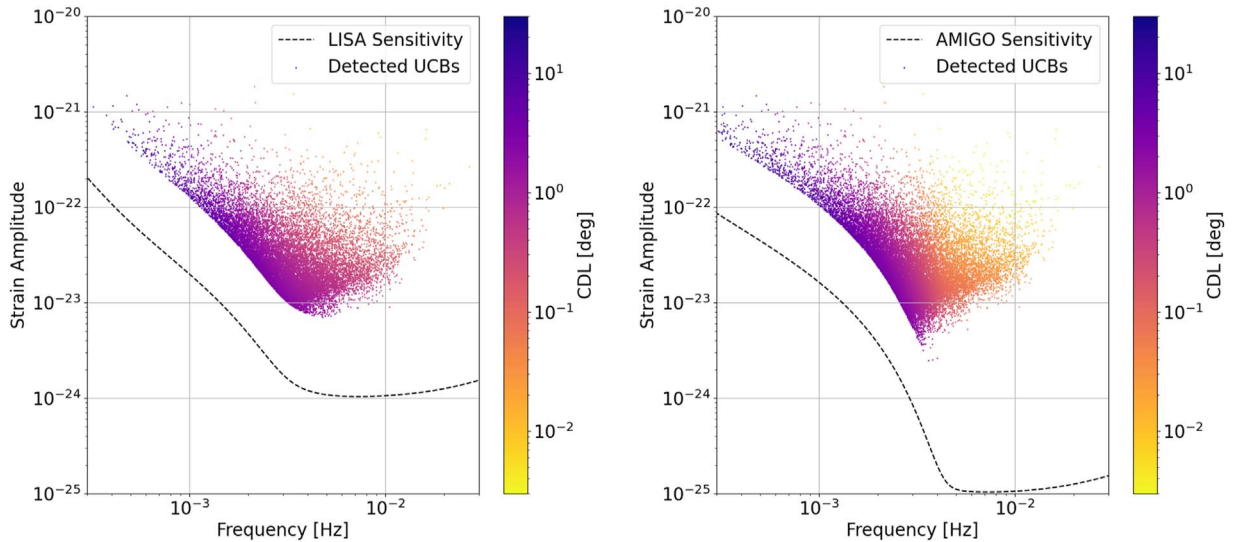


Figure 2. Estimated angular resolution from the coherent diffraction limit for simulated detections with LISA (left, 17,111 systems) and AMIGO (right, 23,245 systems).

UCB sources, in particular the ones with higher signal-to-noise ratio and residing in more sparsely-populated regions of parameter space, will be individually resolved. The remaining unresolved population can be treated as an additional noise source when considering the resolved sources. The solid lines in Figure 1 represent the addition of a GW foreground model from Karnesis et al. (2021) to the instrumental sensitivities. It is worth noting that the amplitude of the confusion noise depends mostly on the duration of the measurement (which determines the frequency resolution) and only weakly on the sensitivity of the instrument once the UCB population becomes detectable. Here we use the same confusion noise model for both LISA and AMIGO, with the result that AMIGO’s improved instrumental sensitivity is only realized for higher frequencies where the confusion noise becomes subdominant.

Using these combined sensitivity curves, we can compute the signal-to-noise ratio (S/N) for each system and apply a threshold to select the systems which will be “detected.” We compute S/N following the formalism in Babak et al. (2021), which accounts for the latest LISA design details and incorporates the Galactic confusion noise model in Karnesis et al. (2021). With a detection criteria of $S/N > 8$, the result is to 17,111 systems for LISA and 23,245 systems for AMIGO. It is this set of resolved sources that we will use to make our image of the Milky Way. In actual practice, each of these individual systems will have to be identified and characterized through template matching. The combined matched-filter search for the entire UCB population is known as the “global fit.” Prototype global-fit codes based on transdimensional Markov chain Monte Carlo algorithms have demonstrated that it is indeed possible to identify tens of thousands of individual signals from a set of simulated instrumental data and make estimates of their relevant parameters (Littenberg & Cornish 2023; Lackeos et al. 2023). The output of the global fit is a multidimensional data set containing parameter estimates for all sources. For many LISA science investigations, these data will be directly compared with models of the underlying source or population of sources. For this work, we are interested in three parameters: the GW amplitude, the GW frequency, and the location of the source on the sky, which will correspond, respectively, to intensity, color, and pixel location

in our image. The first two quantities are directly measured by the instrument with a precision of $\sim S/N^{-1}$. Sky localization for persistent, quasimonochromatic sources such as UCBs arises from modulations in both the observed GW frequency due to the constellation’s orbital motion as well as in the observed GW amplitude from changes in the orientation of the source relative to the constellation (Cutler 1998). The output of a global-fit code describes the probability distribution of these parameters for each source; for example, as a finite set of samples drawn from the estimated distributions. For actual LISA data, or high-fidelity simulations of LISA observations, these data can directly be used to form false-color images. In cases where such data are not available, for example studies of multiple mission configurations and/or Galaxy models, an approximate global-fit output can be synthesized using an approximation method. One approach to such an approximation is to treat the GW observation in an analogous manner to wave optics. In Mandel et al. (2018), the sky localization is estimated as a ratio between the precision with which a feature in the GW waveform can be timed and the light-crossing time of the detector orbit. This idea is extended in the “coherent diffraction limit” (CDL) approximation, which uses the Fisher information matrix approach to estimate the precision with which GW phase can be measured in different positions along the measurement orbit. A full derivation of the CDL, including corrections required for transient sources, will be presented in a future publication. For the case of continuous-wave sources observed with LISA-like instruments in a circular orbit, the CDL estimates the median GW resolution as:

$$\begin{aligned} \sigma_\theta &\approx \frac{\sqrt{2}}{\pi} \rho^{-1} \lambda_{\text{GW}} D^{-1} \\ &\approx 0.11 \text{ rad} \frac{8}{\rho} \frac{f_{\text{GW}}}{1 \text{ mHz}} \frac{2 \text{ A.U.}}{D} \end{aligned} \quad (2)$$

where σ_θ is the variance of the sky location measurement, ρ is the S/N, $\lambda_{\text{GW}} = c/f_{\text{GW}}$ is the GW wavelength, and D is the effective aperture of the GW antenna. For the long-duration LISA observations of Galactic binaries, the orbit of the constellation results in $D = 2 \text{ A.U.}$ Figure 2 shows the

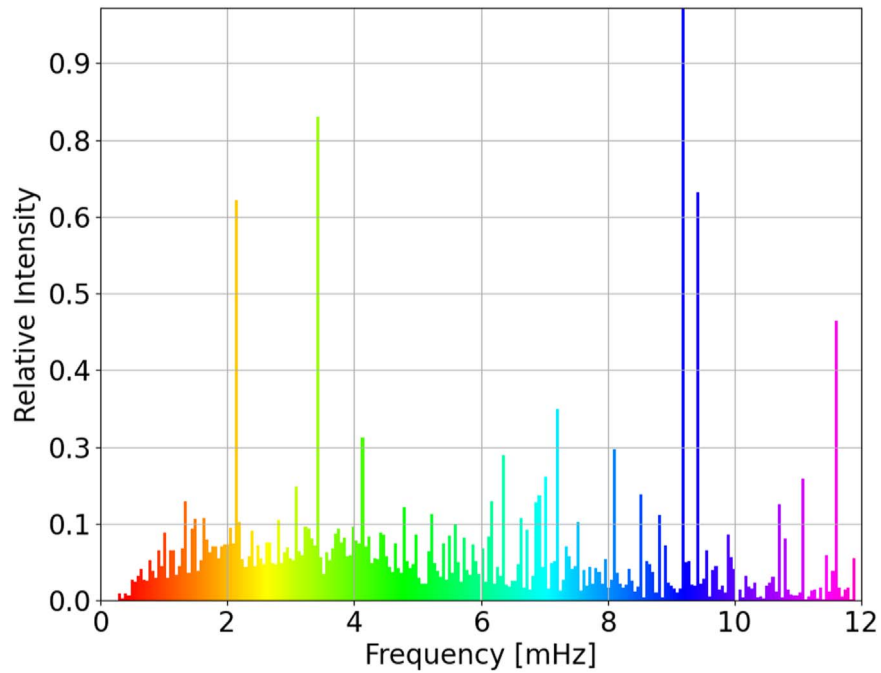


Figure 3. Spectral density of gravitational-wave luminosity for the simulated observations of UCBs with LISA. Luminosity is expressed as relative intensity computed using (4). The `gistainbow` colormap from `matplotlib` is used to color the frequency bins so that the colors match those used in the images below.

estimated angular resolution for each detected source in the frequency-amplitude plane for LISA and AMIGO. AMIGO’s resolving capabilities for UCBs are particularly improved compared to LISA’s for higher-frequency sources where the UCB source confusion contributes less to the overall GW sensitivity than the instrument noise. In [Appendix](#), we present a comparison between the sky position errors for high-fidelity simulations of LISA measurements of UCBs with estimates from the CDL approximation and the resulting impact on image generation. In general, the CDL sets a lower limit on the sky position error estimates from the high-fidelity simulation, with typical values for the high-fidelity errors (which are also generally non-Gaussian) a few times larger. The CDL additionally does not account for correlations between the two sky angles or correlations between sky angles and sky error, which can produce noticeable features in the resulting images.

3. Producing an Image from a Population of GW Sources

The ensemble of UCB sources can be used as a proxy for studying the Milky Way itself, much in the way the light from a large number of atoms or molecules is used to study a star or Galaxy. The difference in this case is that each UCB system is individually detected, albeit with a range of potential parameters such as sky location. Here we describe a method by which the ensemble data set can be used to generate a false-color image that represents GW luminosity as image intensity and GW frequency as color. We begin by taking each of the sources in the ensemble and drawing a set of samples from its measured parameter distribution. In principle, this would include distributions on GW amplitude and frequency as well as sky localization. For this work, we hold the amplitude and frequency fixed for each source and draw sky location samples from a 2D Gaussian centered on the true source position and

with a width given by the CDL-estimated angular resolution. The number of points in the sample is a free parameter for the algorithm, but should be the same for all UCBs above the detection threshold and large enough to smoothly represent the underlying distribution. A sample size of 1000 was used for the images presented here. This sampling process is repeated for each UCB in the ensemble and the samples are concatenated together to make a superensemble of GW measurements. For the case of data from a realistic UCB search pipeline, the samples for each UCB would be drawn from the recovered posterior distribution for each detection, which would not necessarily be Gaussian or even single mode. One way to interpret this process is by analogy to high-energy astrophysics missions where individual photons from a single source are identified and characterized in energy and sky location with source then being reconstructed from the combined ensemble of detected photons. In this qualitative analogy, the GW samples that have either been produced by a search algorithm or simply generated using the CDL estimate, play the role of the “photons.”

The next step in the image-production pipeline is to compute the GW luminosity for each source. For these quasimonochromatic sources, intensity can be estimated as

$$L_{\text{GW}} \propto A_{\text{GW}} f_{\text{GW}}^2 \quad (3)$$

where A_{GW} and f_{GW} are the amplitude and frequency of the GW, respectively. Figure 3 shows a histogram of GW intensities versus GW frequency for the superensemble of simulated LISA detections. The bars of the histograms have been shaded using a linear RGB colormap (`matplotlib`’s `gistainbow`) covering the frequencies from 0 to 12 mHz. This mapping allows the luminosities of each element in the superensemble to be divided into red, green, and blue channels through weighting by the RGB values of the colormap in that bin. For example, with `gistainbow` linearly mapped

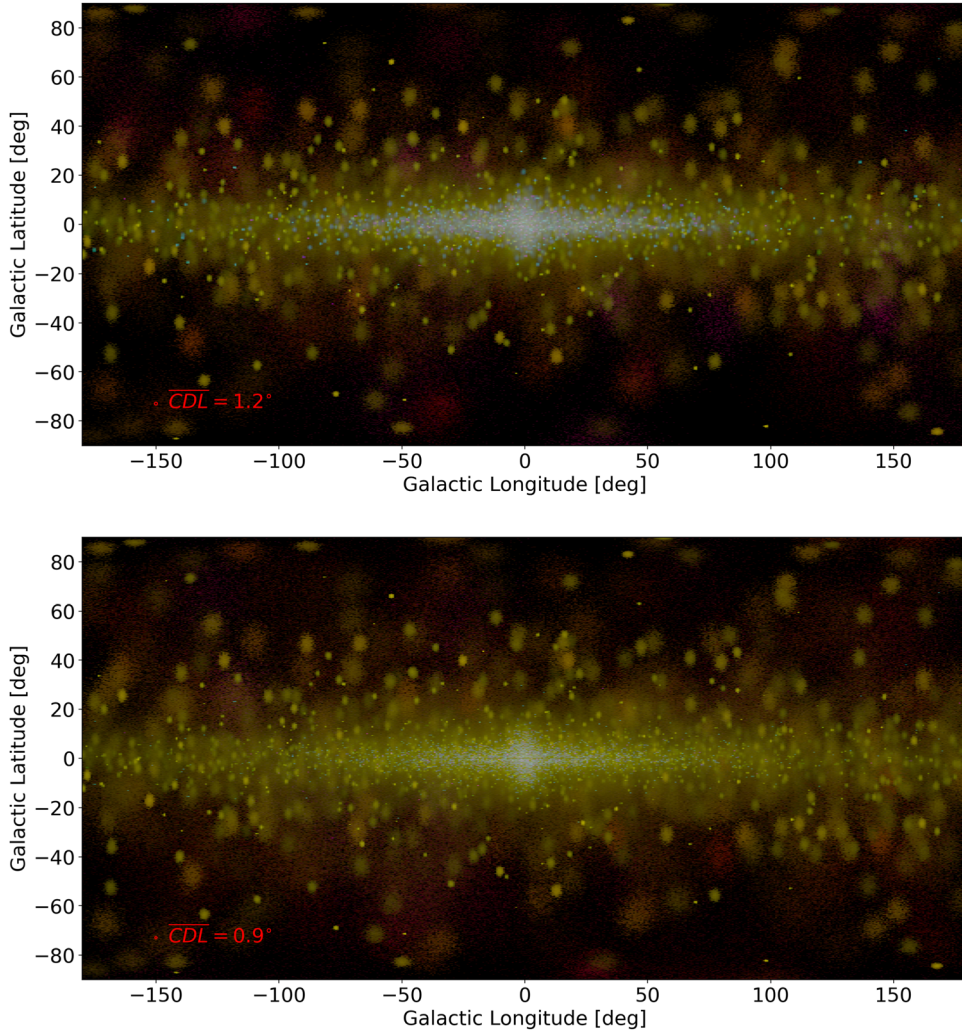


Figure 4. False-color image of simulated LISA (top) and AMIGO (bottom) detections of UCB binaries with one year of data. The size of the median CDL, \overline{CDL} , over all sources is represented by a red circle in each image.

between 0 and 12 mHz, the RGB weightings for the bin centered at 3 mHz are 0.81, 1.00, and 0.00 respectively. The spectrum in Figure 3 shows a distribution of GW energy across the band, with a broad peak in the region of $1 \sim 5$ mHz. This region corresponds to the regime with the greatest number density of detected sources. Rising far above this continuum feature are several sharp lines of varying amplitudes, which represent individual bright sources that are physically close to the detector.

The next step in the image-production algorithm is to grid the sky into a set of bins and estimate the color and intensity for each bin. This could be done with any number of standard binning techniques on the 2-sphere, here we use approximately equal-area bins with even spacing in longitude and cosine of latitude. For each grid, the total luminosity in each of the three color channels is computed by summing the individual RGB values for every element within the bin weighted by the overall luminosity for each element. The false-color image can then be directly represented using this 2D array of RGB values.

In the case of the simulated GW emission from the Milky Way, the dynamic range between the brightest and dimmest

pixels spans more than eight orders of magnitude. To make fainter features more visible, we apply a logarithmic scaling in amplitude. Relative log luminosity is first computed for each pixel by dividing by the luminosity of the greatest pixel and then applying the logarithmic scaling. Zero-luminosity pixels are assigned a log luminosity of ten less than the minimum nonzero pixel. Next, a minimum threshold luminosity is chosen to represent zero intensity in the image. For best results, this should be near the lower end of luminosity in the nonzero pixels.

The final intensity per color channel, i , is then computed for each pixel as:

$$I_i = 1 - \frac{\log \hat{L}_{GW,i}}{\log R} \quad (4)$$

where $\hat{L}_{GW,i}$ is the intensity per channel divided by the maximum intensity across all channels and pixels ($\max(L_{GW})$), and R is the dynamic range of our choice or the fraction of $\max(L_{GW})$ at which we wish to truncate the intensity scale; $R = 10^{-8}$ herein. We then clip I_i to the range $[0, 1]$ to fit within the RGB intensity scale of our plotting software.

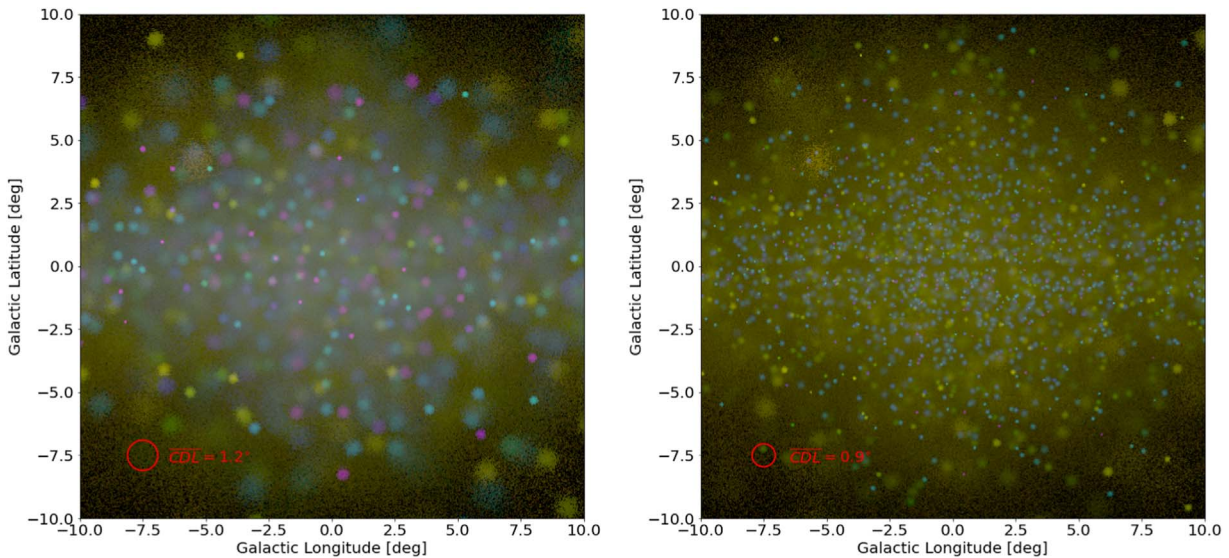


Figure 5. Simulated LISA (left) and AMIGO (right) images for a $10^\circ \times 10^\circ$ region around the Galactic center. The size of the median CDL, \bar{CDL} , over all sources is represented by a red circle in each image.

4. The Milky Way in Millihertz Gravitational Waves

Figure 4 shows the resulting image of the Milky Way using the technique above for simulated observations with both the LISA and AMIGO observatories. Several features of the Galaxy are immediately evident including the Galactic plane and bulge. These features are most prominent in the bluer colors, which correspond to GW sources that are brighter, better-resolved, and at the highest frequencies (systems in the right-hand side of Figure 2). A diffuse yellow glow represents sources at lower frequency and amplitude which are generally not well-localized individually but still trace the basic Galactic structures. Distinct patches of both yellow and bluish colors represent individual sources with the former being generally less well-localized than the latter. The yellow patches in particular likely represent faint nearby UCB sources.

The improved resolving power of AMIGO is more easily demonstrated by comparing the false-color GW images of the Galactic center, where the density of UCB systems leads to source confusion. Figure 5 shows the simulated LISA and AMIGO images for a $10^\circ \times 10^\circ$ region around the Galactic center. The AMIGO image contains many more resolved sources, particularly at the mid-to-high GW frequencies represented in the blue and magenta colors.

5. Discussion

We have outlined a technique for generating false-color images from gravitational-wave observations of a population of individually-detected GW sources in an extended astrophysical object. LISA observations of double white-dwarf systems in the Milky Way will likely be the first such population to be observed and we have produced simulated false-color images that suggest what our Galaxy might look like with LISA “eyes.” This image-generating technique can be directly applied to LISA data, as demonstrated with the high-fidelity simulated data in Appendix. Features in the underlying Galaxy model, such as the Galactic plane and bulge, are directly visible in these images. For real-world data, such images may provide a convenient approach for certain LISA science investigations,

such as identifying potential EM counterparts via cross-matching with other data sets.

While our initial demonstration has focused on images made from the double white-dwarf component of the LISA catalog, the same technique can be applied to other sources and detectors. LISA will also observe neutron star, black hole, and mixed-component binaries in the Milky Way. An image made from these sources might help identify some of the “missing pulsars” in the Galactic center. Advanced detectors such as AMIGO and others, may localize dozens of Galactic binary black holes to within a few degrees or better, making it possible to constrain BBH formation channels by localizing them in the field (isolated binary evolution), in globular clusters or the nuclear cluster of our Galaxy (dynamical formation) or halo (primordial black holes). The technique could also be applied to the large numbers of binary stellar-mass black hole mergers expected to be detected by next-generation ground-based interferometers or an ensemble of supermassive black hole mergers detected by pulsar timing arrays.

Images such as these will provide a novel approach to interpreting gravitational-wave data. In addition, they can be powerful tools for public and scientific outreach by allowing a new and unfamiliar astronomical data set to be cast into a familiar framework.

Acknowledgments

We thank Tyson Littenberg and Kristen Lackeos for access to the products of the GBMCMC search of the LISA Data Challenge 1–4 as well as his helpful comments on the manuscript. C. C. acknowledges support by NASA under award number 80GSFC17M0002.

Appendix Comparison of CDL Estimate with Simulated LISA Detections

While the coherent diffraction limit (CDL) formalism has the advantage of being both intuitive and simple to compute, it does not account for a range of effects that are important in fully understanding the performance of gravitational-wave

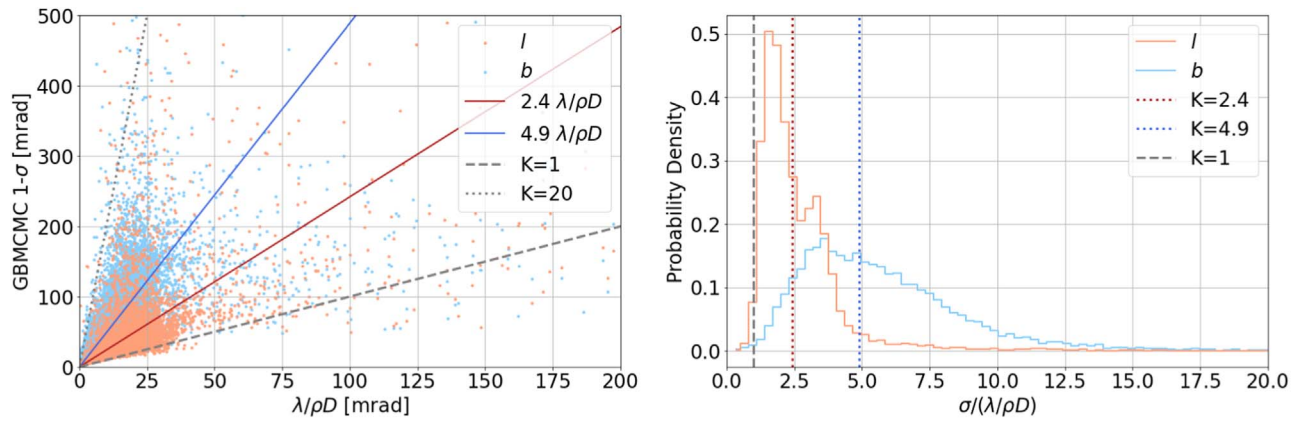


Figure 6. Comparison of GBMCMC 1σ errors and coherent diffraction limit estimates of sky position errors for 10026 Galactic binaries identified in a simulated 12mo LISA observation. The left panel shows scatter plot of latitude and longitude for all sources with reference lines for different scale factors K . The right panel shows histogram of scale factors for latitude and longitude measurements.

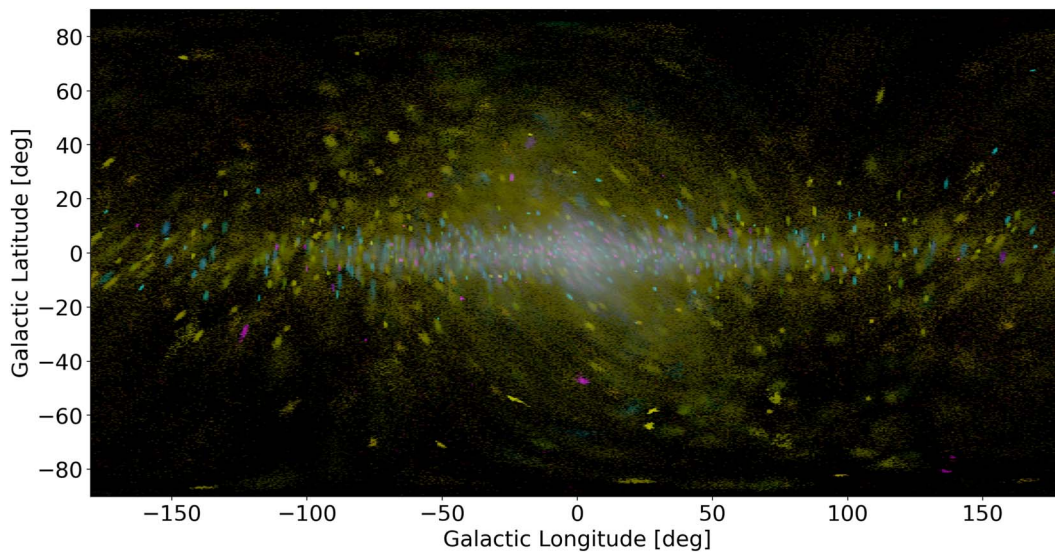


Figure 7. False-color image of LISA detections of 10026 UCB binaries from a high-fidelity simulation of source identification and extraction using GBMCMC as described in Lackeos et al. (2023). Compare with the image made using the coherent diffraction limit in Figure 4.

instruments such as degeneracies between waveform parameters, interactions between multiple sources, etc. For the case of LISA, a number of high-fidelity simulations of the detection and subsequent analysis provide an opportunity to cross-check the CDL estimate. Here we use the results of a search by Lackeos et al. (2023) of a simulated population of LISA-observable Galactic binaries.⁷ The search, known as GBMCMC (Littenberg et al. 2020), uses a transdimensional Markov chain Monte Carlo technique to identify a population of individual sources and estimate full probability distributions of their astrophysical parameters including frequency, S/N, and sky localization. Figure 6 shows a comparison of the sky position errors estimated using (2) with the estimated 1σ errors from the GBMCMC-generated posteriors for both Ecliptic Latitude (b) and Longitude (l) for 10026 individual GB sources extracted from the LDC1-4 data set. A careful reader will note that the number of GBMCMC detections for LISA is smaller by a factor of ~ 2 than the number estimated by a simple $S/N > 8$ threshold applied in Section 2. The likely

reason for this is that the global-fit extraction is not “complete”—systems that meet the S/N threshold are not identified by the search, likely because they are blended with other signals and not individually identified. This confusion effect is especially pronounced at the lower end of the band where the sources are more numerous as seen in Figure 1. In general, the completeness is expected to improve with observation time as the improved frequency resolution will allow individual sources that are closely spaced in frequency to be separately identified.




Since the GBMCMC posteriors are not necessarily Gaussian, we estimated $2\sigma \approx Q_{84} - Q_{16}$ where Q_{84} and Q_{16} are the 84th and 16th percentiles of the sampled posterior, respectively. The scatter plot in the left panel shows that both the latitude and longitude measurements from GBMCMC are well-correlated with the CDL estimates, with the majority of points lying with a range of slopes $1 \leq K \leq 20$. Longitude has a slightly lower slope ($K \approx 2.4$) than latitude ($K \approx 4.9$) which is an illustration of an important effect, possibly caused by the geometry of the LISA constellation and the resulting GW antenna pattern, that is not captured in the simplistic CDL estimate. On the other hand, the CDL estimate required minimal computing cost

⁷ Specifically, the challenge 1–4 data set of the Radler LISA Data Challenge: <https://lisa-ldc.lal.in2p3.fr/challenge1>, which uses the same simulated Galactic population as the rest of this paper.

whereas the GBMCMC run required $\mathcal{O}(10^5)$ CPU-hours (and produced a much richer data set with applications well beyond sky localization). The right panel in Figure 6 shows a histogram of the ratio K between the GBMCMC and CDL estimates for sky localization for both latitude and longitude over all 10026 sources.

Applying the image-generating technique described in Section 3 to the GBMCMC output samples results in the image in Figure 7. While the image is qualitatively similar to the one producing using the CDL estimate (top panel of Figure 4), it exhibits some distinct features such as the “warping” around the ecliptic plane likely caused by the projection of asymmetries in LISA’s localization capability (in-plane of the constellation versus out-of-plane) onto the Galactic plane.

ORCID iDs

Scott Noble  <https://orcid.org/0000-0003-3547-8306>
 Cecilia Chirenti  <https://orcid.org/0000-0003-2759-1368>
 James Ira Thorpe  <https://orcid.org/0000-0001-9276-4312>

References

- Abbott, B. P., Abbott, R., Abbott, T. D., et al. 2016, *PhRvL*, **116**, 061102
 Abbott, R., Abbott, T. D., Acernese, F., et al. 2023, *PhRvX*, **13**, 011048
 Acernese, F., Agathos, M., Agatsuma, K., et al. 2015, *CQGra*, **32**, 024001
 Amaro-Seoane, P., Andrews, J., Arca Sedda, M., et al. 2023, *LRR*, **26**, 2
 Amaro-Seoane, P., Audley, H., Babak, S., et al. 2017, arXiv:arXiv:1702.00786
 Babak, S., Hewitson, M., & Petiteau, A. 2021, arXiv:2108.01167
 Baibhav, V., Barack, L., Berti, E., et al. 2021, *ExA*, **51**, 1385
 Belczynski, K., Kalogera, V., & Bulik, T. 2002, *ApJ*, **572**, 407
 Cutler, C. 1998, *PhRvD*, **57**, 7089
 Einstein, A. 1918, *Sitzungsberichte der Königlich Preußischen Akademie der Wissenschaften* (Berlin: Springer), 154
 Kamesis, N., Babak, S., Pieroni, M., Cornish, N., & Littenberg, T. 2021, *PhRvD*, **104**, 043019
 Keim, M. A., Korol, V., & Rossi, E. M. 2023, *MNRAS*, **521**, 1088
 Korol, V., Hallakoun, N., Toonen, S., & Kamesis, N. 2022, *MNRAS*, **511**, 5936
 Lackeos, K., Littenberg, T. B., Cornish, N. J., & Thorpe, J. I. 2023
 LIGO Scientific Collaboration, Aasi, J., Abbott, B. P., et al. 2015, *CQGra*, **32**, 074001
 Littenberg, T. B., & Cornish, N. J. 2023, *PhRvD*, **107**, 063004
 Littenberg, T. B., Cornish, N. J., Lackeos, K., & Robson, T. 2020, *PhRvD*, **101**, 123021
 Luo, J., Chen, L.-S., Duan, H.-Z., et al. 2016, *CQGra*, **33**, 035010
 Mandel, I., Sesana, A., & Vecchio, A. 2018, *CQGra*, **35**, 054004
 Nelemans, G., Yungelson, L. R., & Portegies Zwart, S. F. 2001, *A&A*, **375**, 890
 Nisanke, S., Vallisneri, M., Nelemans, G., & Prince, T. A. 2012, *ApJ*, **758**, 131
 Ruan, W.-H., Guo, Z.-K., Cai, R.-G., & Zhang, Y.-Z. 2020, *IJMPA*, **35**, 2050075
 Toonen, S., Nelemans, G., & Portegies Zwart, S. 2012, *A&A*, **546**, A70
 Wagg, T., Broekgaarden, F. S., de Mink, S. E., et al. 2022, *ApJ*, **937**, 118
 Yu, S., & Jeffery, C. S. 2010, *A&A*, **521**, A85